ADVANCED MATERIALS
www.advmat.de

Close-Loop Cathode Chemistry Enables Self-Rejuvenating Aqueous Zn–Te Batteries Compromised by Non-Equilibrium Redox Pathways

Rui Pan, Yucheng Xie, Bowen Jiang, YingYu Han, Andreu Cabot, Zhenjing Jiang, Guoju Zhang, Zhipeng Shao, Shulin Jiao, Litao Sun, Kuibo Yin,* and Qichong Zhang**

Tellurium (Te) emerges as an alluring cathode material for aqueous zinc-ion batteries, boasting an unrivaled six-electron-transfer capacity (1260 mAh g^{-1} and 7829 mAh cm^{-3}). However, the battery performance and cycling stability are severely degraded by inherent $TeO_x{\cdot}H_2O$(aq) shuttle arising from proton-tunneling-induced non-equilibrium electrochemical hydrolysis, where proton-coupled electron transfer (PCET) dominates. In this work, a rejuvenation of dead Zn–Te batteries is demonstrated based on a close-loop chemistry via employing organic triethylsulfonium iodide ($C_6H_{15}SI$, TESI). The triiodide anions (I_3^-) are found to reduce dissolved $TeO_x{\cdot}H_2O$(aq.) with thermodynamic favorability to revitalize Te cathode, meanwhile, generated I_2 is recycled back into the electrolyte by reacting with iodide anions. Simply left resting for 12 h, a completely degraded Zn–Te cell (1500 cycles) recovered 94.3% of its initial capacity (465 mAh g^{-1}). Furthermore, TES^+ is found to promote an anode solid electrolyte interphase via detaching ethyl. The functional layer efficaciously prevented anode passivation caused by tellurium-shuttling and facilitated efficient zinc-ion transfer to achieve dendrite-free zinc anode. This loop chemistry not only extends the lifespan of batteries but also enables the reuse of materials, potentially reducing the overall cost of battery production and resource consumption.

1. Introduction

Aqueous zinc–tellurium (Zn–Te) batteries have emerged as a highly promising alternative to conventional lithium-ion batteries, offering inherent safety from non-flammable aqueous electrolytes, an exceptional theoretical capacity (1260 mAh g^{-1}) enabled by the six electron transfer ($Te^{2-}/Te^0/Te^{4+}$), and high intrinsic electrical conductivity (2×10^2 S m^{-1}).[1–4] These attributes position Zn–Te systems as strong candidates for next-generation energy storage.[5–7] However, the practical deployment of tellurium-based cathodes faces significant challenges that mirror those of other metal-chalcogenide battery systems.[8–14] The most critical limitation stems from the high solubility of tellurium and its intermediate species in aqueous electrolytes. This dissolution leads to three interrelated failure mechanisms: 1) irreversible active material loss from the cathode, 2) rapid capacity fading due to disrupted redox pathways, and 3) severe parasitic self-discharge through redox shuttle effects.[2] These issues are particularly pronounced in the mild acidic to neutral pH range typically employed in Zn-based battery systems, where tellurium species exhibit enhanced solubility and mobility.[2,4,15–17] Despite its critical importance, the poorly understood shuttling mechanism remains a key barrier to realizing the full potential of aqueous Zn–Te batteries.

Current mitigation strategies primarily focus on stabilizing redox processes through two approaches. First, cathode

R. Pan, B. Jiang, Z. Jiang, G. Zhang, L. Sun, K. Yin
SEU-FEI Nano-Pico Center
Key Laboratory of MEMS of Ministry of Education
Southeast University
Nanjing 210096, China
E-mail: yinkuibo@seu.edu.cn

Y. Xie, Y. Han, Z. Shao, Q. Zhang
Key Laboratory of Multifunctional Nanomaterials and Smart Systems
Suzhou Institute of Nano-Tech and Nano-Bionics
Chinese Academy of Sciences
Suzhou 215123, China
E-mail: qczhang2016@sinano.ac.cn

S. Jiao
Collaborative Innovation Center of Advanced Microstructures Laboratory of Solid State Microstructures and School of Physics
Nanjing University
Nanjing 210093, China

A. Cabot
Catalonia Energy Research Institute-IREC
Sant Adrià de Besòs
Barcelona, Catalonia 08930, Spain
E-mail: acabot@irec.cat

A. Cabot
ICREA
Pg. Lluis Companys 23, Barcelona, Catalonia 08010, Spain

The ORCID identification number(s) for the author(s) of this article can be found under https://doi.org/10.1002/adma.202519737

DOI: 10.1002/adma.202519737

engineering employs physical confinement methods such as carbon-coated ZnTe nanowires to trap soluble intermediates,[18] while catalytic designs like hierarchical MnO@C structures aim to accelerate redox kinetics and reduce intermediate migration.[19] However, these methods fail to address the fundamental issue of proton-coupled electron transfer (PCET)-driven hydrolysis intrinsically common to conversion-type cathodes like Te,[1,2,4] S,[20,21,22] Se[23] and MnO_2.[24–29] In aqueous batteries, PCET underpins key redox processes (proton insertion, hydrolysis-driven conversion, redox of oxyanions)[30–32] and explains pH-dependent voltages shifts. Yet, the quantum nature of proton tunneling complicates control, inducing interfacial pH instabilities. By bypassing high-energy charged intermediates and lowering overpotentials, proton tunneling can redirect reaction pathways toward parasitic or non-equilibrium routes.[33] This not only undermines reversibility but also leads to discrepancies between mechanisms inferred from ex situ and in situ characterizations conducted on different timescales (Table S1, Supporting Information).[34,35] A more direct strategy involves electrolyte engineering to mitigate undesirable water participation reactions itself, even though, paradoxically, these same reactions are essential for achieving the high capacity enabled by PCET-promoted multi-electron redox processes. Zhang et al. demonstrated that an acetate-rich electrolyte can confine free water molecules and buffer pH, thereby promoting rapid amorphous TeO_2 formation; however, the reduced availability of interfacial water limits the accessible capacity and exacerbates Zn corrosion.[36] An alternative approach utilizing highly concentrated 30 M $ZnCl_2$ goes beyond simple water suppression by activating hypervalent chemistry ($ZnTe + 8Cl^- + 6e^- \rightarrow TeCl_4 + ZnCl_4 2^-$) at the Te cathode, achieving an ultrahigh capacity of 1223.9 mAh g_{Te}^{-1}.[2,37] Further refinement showed that modifying such $ZnCl_2$-based electrolytes with ionic liquid and ethylene glycol (EG) enhances the system through the strong nucleophilic Cl^- anion, which simultaneously improves multivalent conversion reactions and suppresses Te^{n+} dissolution/decomposition.[37]

However, while the nucleophilic Br^- or Cl^- facilitates hypervalent chemistry, it introduces several drawbacks: reduced cathode conductivity, formation of problematic metastable γ-TeO_2 phases that worsen material shuttling (though glucose additives can partially mitigate this effect), and additional complications including diffusible $TeCl^{3+}$ intermediates and water susceptibility.[1,38] These Cl^-/Br^--based concentration methods also present practical challenges such as increased viscosity, higher costs, and long-term stability concerns. Importantly, none of these approaches fully resolves the detrimental impact of electrochemical tellurium hydrolysis on the zinc anode.

Herein, we focus on the critical trade-off that fundamentally governs Zn–Te battery performance: In situ electrochemical activation of Te via PCET processes, a strategy long regarded solely as beneficial for cathode performance improvement,[20,39,40] unlocks high-capacity redox pathways but also accelerates Te dissolution and material loss via non-equilibrium pathways because of dynamic protonation. The dissolvable tellurium species are found to primarily exist as neutral, high-valence $TeO_2 \cdot H_2O$(aq) and $TeO_3 \cdot H_2O$(aq) complexes, formed through electrochemical water-participation and intercalation oxidation pathways ($Te(s) + 3H_2O - 4e^- \rightarrow TeO_2 \cdot H_2O(aq) + 4H^+$ and $Te(s) + 4H_2O - 6e^- \rightarrow TeO_3 \cdot H_2O$ (aq) + $6H^+$). These mobile species shuttle to the zinc anode, where they induce passivation through the reaction $TeO_3 \cdot H_2O + 4Zn \rightarrow ZnTe + 3ZnO + H_2O$, ultimately leading to battery overcharge and failure at practical active material loadings (>5 mg cm^{-2}) (**Scheme 1**). To address these challenges, we propose a closed-loop chemistry system using organic triethylsulfonium iodide (TESI, $C_6H_{15}SI$). During operation, TESI generates triiodide anions (I_3^-) that thermodynamically favor the reduction of dissolved $TeO_x \cdot H_2O$(aq) species, effectively dynamically regenerating the Te cathode according to Le chatelier principle. Simultaneously, any formed I_2 is efficiently recycled via reaction with iodide anions (I^-) when left rest, completing the redox cycle. This innovative mechanism enables remarkable cyclability and capacity recovery. Additionally, the TES^+ cation plays an equally critical role by facilitating the formation of a robust solid electrolyte interphase (SEI) on the zinc anode. Through ethyl detachment, TES^+ creates a functional protective layer that prevents tellurium-induced anode passivation, enables efficient Zn^{2+} transport, and promotes dendrite-free zinc deposition. These synergistic effects significantly enhance overall battery cyclability. This closed-loop chemistry represents a major advancement in aqueous zinc-ion battery technology, extending battery lifespan through active material regeneration, reducing production costs via material reuse, and decreasing resource consumption. Beyond device performance, we reveal a non-equilibrium PCET pathway that acts as a double-edged sword: in Zn–Te and Zn–MnO_2 systems it enables high-capacity redox yet simultaneously drives dissolution and shuttling due to proton tunneling effect, offering a unified framework that reconciles inconsistencies between in situ and ex situ observations.

2. Results and Discussion

The tellurium cathode material was synthesized through hydrothermal reduction of sodium tellurite with hydrazine, producing microrod structures composed of Te filaments as confirmed by **Figure 1a**; Figure S1 (Supporting Information). To evaluate their electrochemical performance, aqueous Zn-Te cells were assembled using 2 M $ZnSO_4$ electrolyte in an open two-electrode configuration. Remarkably, upon activation by deep cycling at 0.2 A g^{-1}, the electrode exhibited a near doubling of capacity, increasing from 409 to 882 mAh g^{-1} (Figure S2a, Supporting Information). This value significantly exceeds the theoretical capacity of a two-electron redox mechanism ($Te + 2e^- \rightarrow Te^{2-}$, 425 mAh g^{-1}) but remains below the six-electron pathway involving TeO_2 reduction ($TeO_2 + 6e^- + 4H^+ \rightarrow Te^{2-} + 2H_2O$, 1101 mAh g^{-1}). These results suggest a gradual electrochemical oxidation of Te during cycling, likely transitioning from a two-electron to a mixed multi-electron redox process. Under a higher current density of 0.4 A g^{-1}, the system demonstrated limited cyclability, sustaining only 28 cycles before failure (Figure 1b), accompanied by visible diffusion of black-colored tellurium species across the cell (Figure S2d, Supporting Information).

Comprehensive characterization revealed multiple aspects of the degradation mechanism. Inductively coupled plasma optical emission spectroscopy (ICP-OES) and Raman spectroscopy were used to quantify dissolved Te and analyze its structural evolution (Figure 1c). ICP-OES revealed a monotonic increase of

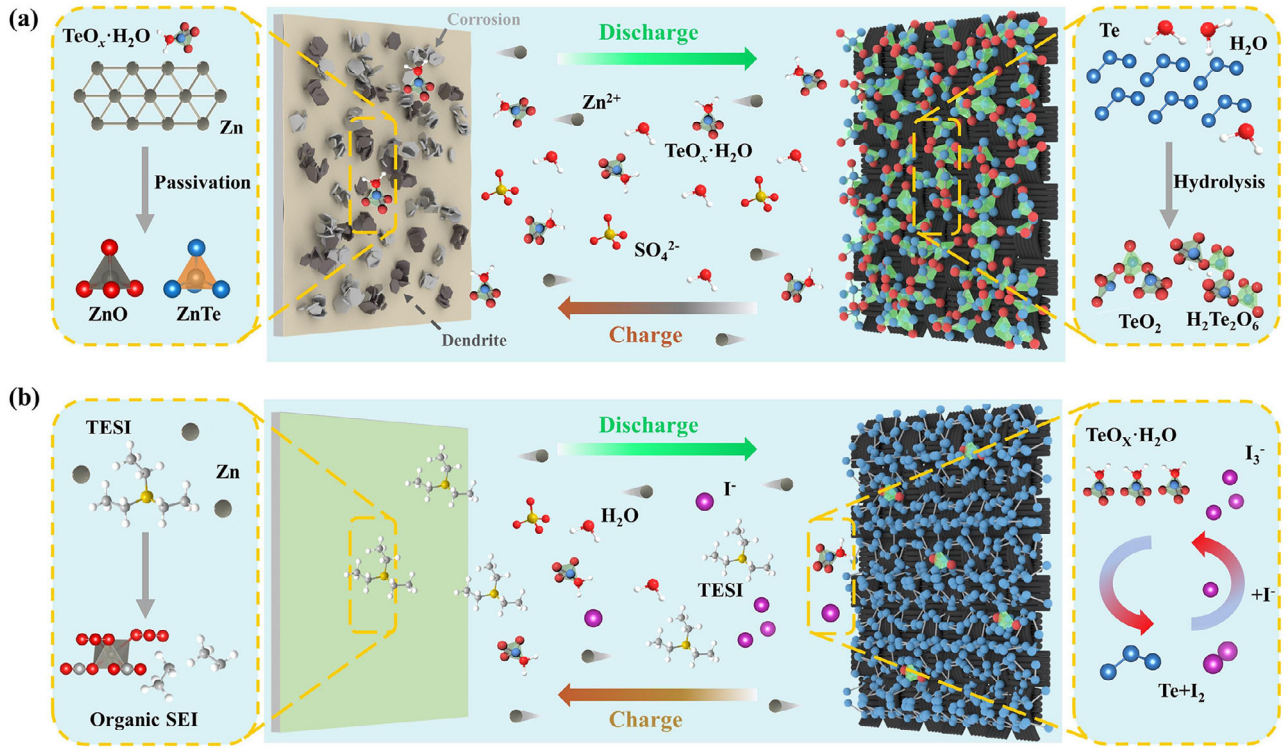

Scheme 1. a) Shuttle and passivation effect induced by $TeO_x{\cdot}nH_2O$ species in the aqueous Zn–Te battery. b) Triple-function TESI additive addressing shuttle issues through functional anode SEI, catalyzing Te redox kinetics, and self-regenerative chemistry in aqueous Zn–Te battery.

the Te concentration in aqueous-phase throughout the activation process, unambiguously confirming progressive tellurium dissolution. Besides, an obvious blue shift of all Raman vibrational peaks is noticed after cycling, further corroborating increased oxidation state of tellurium, consistent with material loss from the cathode. Ex situ X-ray diffraction (XRD) analysis provided additional insights into the phase evolution of the Te cathode. Most of Te diffraction peaks remained discernible but exhibited markedly reduced intensity upon repeated oxidizing (Figure 1d; Figure S3a, Supporting Information), indicative of progressive amorphorization induced by electrochemical restructuring, a phenomenon commonly associated with enhanced electrode kinetics.[20,39–41] Notably, the (001) peak at 23° (characteristic of pristine Te) virtually disappeared post-oxidation, while a new low-angle reflection emerged at ≈8.2°. This shift is attributed to water intercalation into the Te lattice, forming a hydrated intermediate phase ($Te{\cdot}nH_2O$). Concomitantly, the diffraction peaks at 29.2°, 35.6°, and 37° can be indexed as TeO_2 and another two sitting at 12° and 14° are ascribed to $H_2Te(+5)_2O_6$. Both are generated by water-mediated oxidation of Te. High-resolution transmission electron microscopy (HRTEM) was employed to track the structural evolution of tellurium during electrochemical oxidation. As shown in Figure 1e,f, pristine hexagonal Te exhibits a highly crystalline structure with clear (101) lattice fringes, consistent with previous reports.[42] After 10 cycles and charging to 1.25 V, a new lattice fringe indexed to the (400) plane of TeO_2 appears, accompanied by amorphization and defect formation, in agreement with the XRD results. Upon further oxidation to 1.5 V, the fraction of amorphous phase increases significantly (Figure S3b, Supporting Information).

To probe the electronic structure, electron energy loss spectroscopy (EELS) was carried out. As shown in Figure S3c (Supporting Information), pristine Te and reference TeO_2 exhibit distinct sharp peaks at ≈41.3 and ≈44.5 eV, respectively, serving as reliable benchmarks. In contrast, samples collected after the 10th cycle (charged to 1.35 V) and the 13th cycle (charged to 1.6 V) display two additional peaks at higher energy losses of 46.4 and 48.3 eV, which correspond to Te^{5+} and Te^{6+} species.[43] These chemical shifts arise because the electrons of Te at higher oxidation states are more strongly bound to the nucleus due to the increased effective nuclear charge, thus requiring greater excitation energy from the incident beam.

Unlike TeO_2, which can crystallize into an extended lattice, the higher-valence products (e.g., $H_2Te_2O_6$) typically form molecular acids and related complexes, solidifying into amorphous, glass-like phases in aqueous environments. This crystalline-to-amorphous transition of Te during cycling is driven by a drastic reduction in atomic radius and the formation of stronger, more covalent Te—O bonds, which impose severe local lattice strain and disrupt long-range structural coherence (Table S2, Supporting Information). Additional coordination changes exacerbate this mismatch, leading to oxygen vacancies and under-coordinated Te atoms (verified by ex situ EPR, Figure S3d, Supporting Information). The proposed dissolved tellurium species are consistent with thermodynamic predictions from the Pourbaix diagram (Figure 1g).

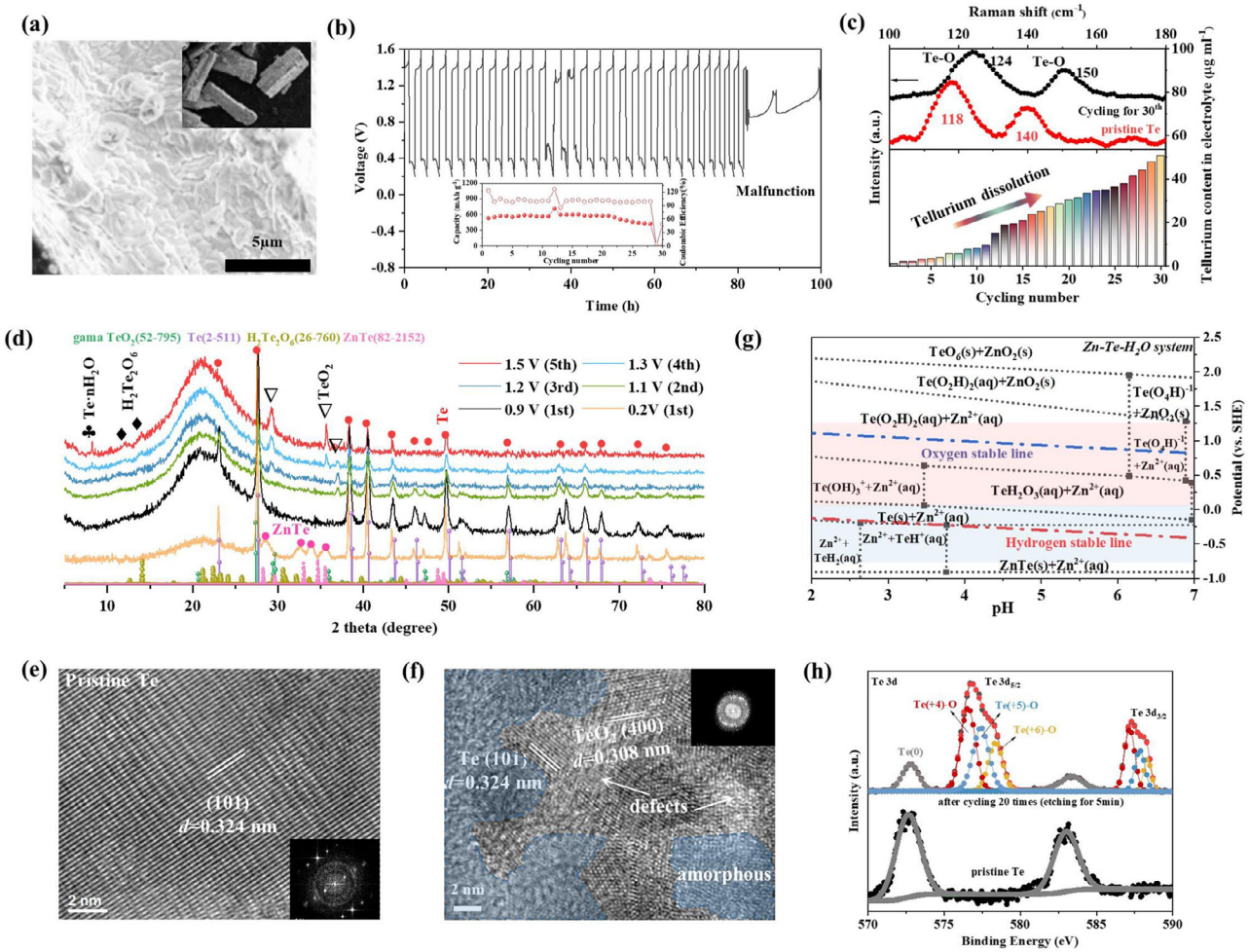

Figure 1. Shuttling mechanism of aqueous Zn–Te battery. a) SEM morphological images of synthesized Te microrod. b) GCD curve of Zn-Te cell at current density 0.4 A g^{-1} with a mass loading of active Te to be ≈5 mg cm^{-2}. Inset: Corresponding cycling performance of Zn-Te cell. c) Raman spectra of the pristine and cycled Te cathode (charged to 1.6 V) and Concentration of dissolved tellurium species in the electrolyte measured at different cycle numbers. d) Ex situ XRD pattern of Te structural changes during cycling. HRTEM images of e) pristine Te and f) cycled Te electrode (charged to 1.25 V) after 10 cycling times, inset: Fast Fourier transform of TEM images. g) Pourbaix diagram of Zn-Te-H_2O system. h) XPS spectra of pristine Te and Te cathode charged to 1.6 V after cycling for 20 times.

According to these results, the proposed electrochemical PCET equilibrium redox pathways are:

$$Te + 2H_2O - 4e^- \rightarrow TeO_2 + 4H^+ \quad (1)$$

$$Te + 3H_2O - 4e^- \rightarrow H_2TeO_3 + 4H^+ \quad (2)$$

$$2Te + 6H_2O - 10e^- \rightarrow H_2Te_2O_6 + 10H^+ \quad (3)$$

$$Te + 6H_2O - 6e^- \rightarrow H_6TeO_6 + 6H^+ \quad (4)$$

These mechanisms parallel Mn^{2+}/MnO_2 redox chemistry (e.g., $Mn^{2+}+2H_2O+2e^- \rightarrow MnO_2+4H^+$), where proton concentration critically governs PCET reaction thermodynamics. Specifically, the Te oxidation potential exhibits a positive correlation with $[H^+]$, prompting validation experiments using acidic electrolytes (elevated $[H^+]$) and anion-exchange membranes. As clearly shown in Figure S4a (Supporting Information), increasing proton concentration leads to ≈0.1 V potential elevation, close to the theoretical value of 0.11 V from the Nernst equation of TeO_2/Te reaction. The critical role of water was demonstrated by comparing Zn–Te batteries in different electrolytes: 2 M $ZnSO_4$ and 2 M $ZnSO_4$/ethylene glycol(EG.) The latter delivered a markedly reduced capacity, confirming that water is an indispensable reactant for Zn–Te battery operation (Figure S4b, Supporting Information).[44] During electrochemical activation, the anodic processes reactions (Te oxidation) can similarly generate protons, in situ pH measurement was conducted at different charged state of Te with varying loadings. The deviation between experimental and theoretical pH values indicates that interfacial protonation dominates over bulk proton diffusion (Figure S4c, Supporting Information), which critically underlie the reversibility of aqueous Zn–Te battery. However, this interfacial high $[H^+]$ environment increases the theoretical Te/Te^{n+} redox potentials, rendering Te/Te^{6+} unavailable. Yet higher $[H^+]$ contributes to localized protonation of Te(IV) species (e.g., electrophilic $HTeO_2^+$),

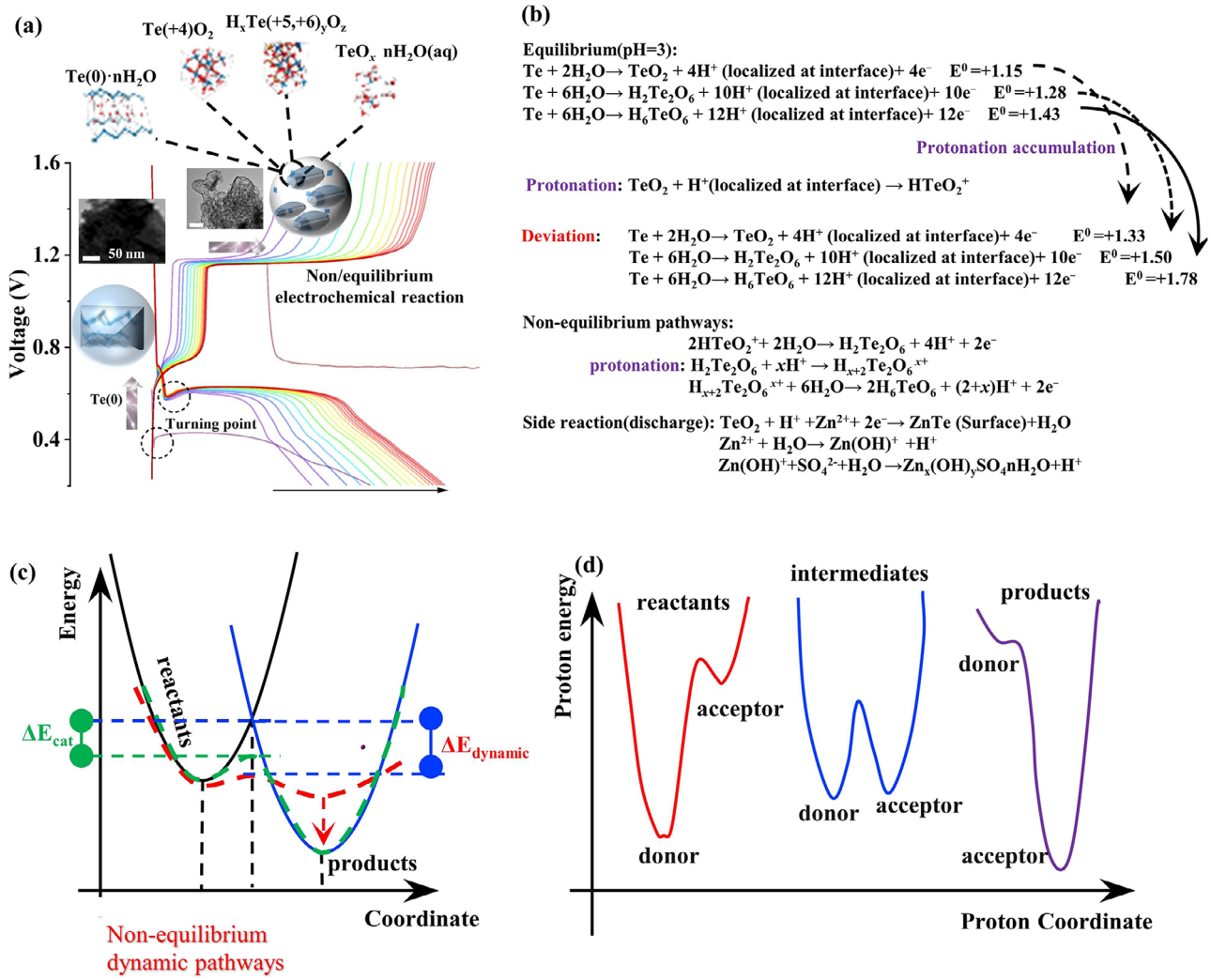

Figure 2. a,b) Illustration and equations portraying the non/equilibrium electrochemical redox pathways of Te that are induced by localized dynamic protonation, which causes capacity decay, energy loss, tellurium shuttle, and anode passivation. Inset: TEM images of the pristine Te and Te after cycling 20 times are also displayed. c) Free energy scheme for the reactants and products as a function of reaction coordinate based on Marcus theory, with possible PCET-promoted non-equilibrium reaction pathways marked in red dot line and conventional catalytic processes marked in green. d) Schematic proton potentials for the reactants, intermediates, and products. (PCET can be described as a vibronic transition between reactant and product states where the transferring electron and proton are treated quantum mechanically and the other reactant nuclei and solvent are treated classically.). PCET mechanisms, particularly those enabled by proton tunneling, can fundamentally alter the landscape of an electrochemical reaction, shifting the dominant factor from thermodynamics to kinetics. This can allow PCET-induce non-equilibrium pathways to bypass both conventional uncoupled pathways and other electro-catalytic cycles.

thereby accelerating nucleophilic attack by water and facilitates Te oxidization, but the accompanied proton tunneling effect drives oxidation behavior to deviate from the equilibrium redox pathways. Those resulted proton-assisted intermediates establish multi-step non-equilibrium pathways (such as Te → TeO_2 → $HTeO_2^+$ → $HTeO_3^+$ → H_6TeO_6) that are less accessible at high [H^+] (**Figure** 2a,b; Table S3, Supporting Information).[16] Notably, PCET has intermediate energy barriers, lower than pure electron transfer of conventional electrochemistry because the concerted transfer of proton and electron avoids high-energy charged intermediates (e.g., cation radicals), reducing the effective reorganization energy and thermochemical bias. In water, proton transfer can be facilitated by Grotthuss mechanisms along water chains, further lowering the barrier compared to decoupled steps.[45] A decrease in water content leads to the suppression of non-equilibrium redox pathways. This results in a shift of the Te/TeO_2 conversion mechanism back to the equilibrium route, which is characterized by an elevated activation potential (Figure S4b, Supporting Information). Electro-catalytic model has the smaller barriers to PCET because catalysts stabilize transition states, provide alternative inner-sphere pathways, break scaling relations between intermediates, and minimize overpotentials. Thus, catalysis is a go-to solution to minimize losses caused by PECT processes.

As further evidenced by the high-resolution Te 3d X-ray Photoelectron Spectroscopy (XPS) spectra (Figure 1h), the increased

valence state of tellurium (+4, +5, and +6) post-activation confirms its electrochemical oxidation to produce high-valence products, in agreement with HRTEM, XRD, and Raman analysis (Figure S4d, Supporting Information). Thermodynamic and kinetic considerations support the reaction in aqueous environments. The Gibbs free energy change (ΔG_f°) for the oxidation of tellurium to tellurium dioxide, i.e., $Te(s)+O_2(g)\rightarrow TeO_2(s)$ is –270.0 kJ mol^{-1} at 298 K. This means the oxidization of Te is thermodynamically favorable. When exposed to humid air or aqueous electrolytes, O_2 readily dissolves in the thin water layer adsorbed on the Te surface, facilitating transport of oxidants to the reactive sites and accelerating Te oxidation. This is consistent with fine Te 3d XPS analysis of pure Te exposed to humid air for 14 days (Figure S3e, Supporting Information), which shows formation of oxidized tellurium state.

To elucidate the charge state of dissolved species, ion-selective membrane experiments were conducted. Notably, Zn–Te batteries exhibited rapid failure irrespective of the membrane type (Figure S2b,c, Supporting Information), unequivocally indicating the dominance of neutral tellurium species (e.g., $TeO_3{\cdot}H_2O$(aq) and minor $TeO_2{\cdot}H_2O$(aq)) in the electrolyte. Consistent with thermodynamic predictions from the Pourbaix diagram (Figure 1g), the solubility of Te species correlates with the formation of hydrated oxides. These neutral species migrate to the Zn anode, triggering passivation via the reaction:

$$TeO_3 \cdot H_2O + 4Zn \rightarrow ZnTe + 3ZnO + H_2O \quad (5)$$

As validated in Figure S5 (Supporting Information).

The interplay of dissolution, migration, and anode passivation underpins the observed electrochemical degradation, with the possible non/equilibrium Te redox pathway summarized schematically in Figure 2b–d. The established non-equilibrium pathways contribute to a shuttle effect in Zn–Te batteries where the dynamic protonation-driven kinetics highlight how interfacial conditions can override bulk thermodynamics to define redox chemistry., analogous to that in lithium–sulfur systems.[11] This non-equilibrium mechanism rationalizes the discrepancy between ex situ and in situ observations in aqueous Zn–Te, Zn-MnO_2 and even Zn-V_2O_5 batteries, where ex situ characterizations reveal proton intercalation along with Zn^{2+} insertion and the formation of crystalline/amorphous Mn_xO_y or Te_mO_n products, while in situ techniques capture only proton intercalation as the dominant process without confirming electrode dissolution (Figures S6 and S7, Table S1–S4, Supporting Information). Notably, the common turning points stem from entropy/Gibbs free energy changes ($\Delta G = \Delta H\text{-}T\Delta S$) in multistep conversion steps highlighting uncontrollable protonated intermediates, analogue to Li-S systems that share similar GCD curves but the entropy increase caused by uncontrollable polysulfide chains.[11]

To extend the lifespan of Zn–Te batteries, resolving anode passivation constitutes the foremost challenge. Constructing an artificial SEI emerges as a promising strategy for practical systems, as it enables regulated Zn^{2+} flux through tailored ion diffusion pathways and lowered desolvation energy barriers, while simultaneously screening solvent molecules (e.g., water). These combined effects suppress parasitic side reactions (e.g., hydrogen evolution and dendrite formation), thereby homogenizing current density distribution and guiding spatially uniform, dendrite-free Zn deposition.[46] Critically, the engineered SEI also acts as a corrosion-resistant barrier, mitigating irreversible anode degradation caused by dissolved Te species ($TeO_3{\cdot}H_2O$(aq) and minor $TeO_2{\cdot}H_2O$(aq)) during cycling. The organic triethylsulfonium iodide additive ($C_6H_{15}SI$, TESI) was selected for its ability to dissociate into iodide anions (I^-) and triethylsulfonium cations (TES^+). The low-lying lowest unoccupied molecular orbital (LUMO) of TES^+ facilitates ethyl group cleavage, enabling in situ generation of a compact and ion-conductive solid electrolyte interphase SEI on the Zn anode. This SEI homogenizes Zn^{2+} flux, suppresses dendrite growth, and mitigates parasitic reactions, as validated in **Figure 3a**.

To evaluate the efficacy of electrolyte additives in mitigating Zn anode degradation, Zn/Zn symmetric cells were assembled with three distinct electrolytes: baseline 2 M $ZnSO_4$, 2 M $ZnSO_4$/25 mM ZnI_2, and 2 M $ZnSO_4$/50 mM TESI. Under high zinc utilization (80% depth of discharge), the cell incorporating the TESI additive exhibited superior electrochemical rate performance, achieving a minimal voltage hysteresis of < 100 mV at a current density of 8 mA cm^{-2} (Figure 3b). This performance markedly outperformed both the additive-free baseline and the ZnI_2-modified electrolyte, underscoring the unique capability of TESI to stabilize Zn plating/stripping under extreme cycling conditions. When cycled at 5 mA cm^{-2} and 10 mAh cm^{-2}, the TESI-modified cell exhibited exceptional durability, enduring 2100 h with stable voltage hysteresis. In stark contrast, cells employing ZnI_2 or unmodified $ZnSO_4$ suffered premature failure via short-circuiting within 400 h (Figure 3c). Electrochemical impedance spectroscopy (EIS) after 20 cycles further corroborated efficacy of TESI, the TESI-enhanced cell demonstrated attenuated charge transfer resistance (R_{ct}), attributable to its homogenized SEI layer, while ZnI_2 and baseline electrolytes exhibited markedly elevated interfacial impedance (Figure 3d). These results underscore the central role of TESI in stabilizing Zn electrodeposition and benefiting superior electrode kinetics.

The composition and spatial distribution of the artificial SEI were systematically analyzed via SEM and XPS equipped with Ar^+ ion beam etching. SEM-EDS mapping (Figure 3e) revealed a homogeneous distribution of Zn, C, and S throughout the SEI layer, with negligible Te content, undoubtedly confirming the effectiveness of SEI in blocking $TeO_3{\cdot}H_2O$(aq) and $TeO_2{\cdot}H_2O$(aq) migration and subsequent anode passivation. High-resolution C 1s XPS spectra (Figure 3f; Figure S8a, Supporting Information) further unveil the carbon-rich organic-inorganic composite structure of SEI. Notably, the oxygen content exhibited a depth-dependent gradient from 3D TOF-SIMS (Figure 3g) and XPS ething analysis, decreasing from the SEI surface to the Zn interface after prolonged etching. This oxygen gradient synergizes with the carbon matrix to facilitate Zn^{2+} desolvation by weakening H_2O-Zn^{2+} coordination and suppress parasitic reactions (e.g., water corrosion and Te-induced passivation), thereby stabilizing the Zn anode during prolonged cycling.

The central challenge and chance are that the conversion between Te and TeO_2 in aqueous electrolytes can proceed via a PCET pathway that demonstrates a lower energy barrier, but the inherent proton tunneling leads to the dissolution and tellurium shuttle. Beyond TESI's role in SEI formation, iodide anions (I^-) are well-documented catalysts in aqueous metal/S and metal/Se battery systems, enhancing redox kinetics via halogen-mediated

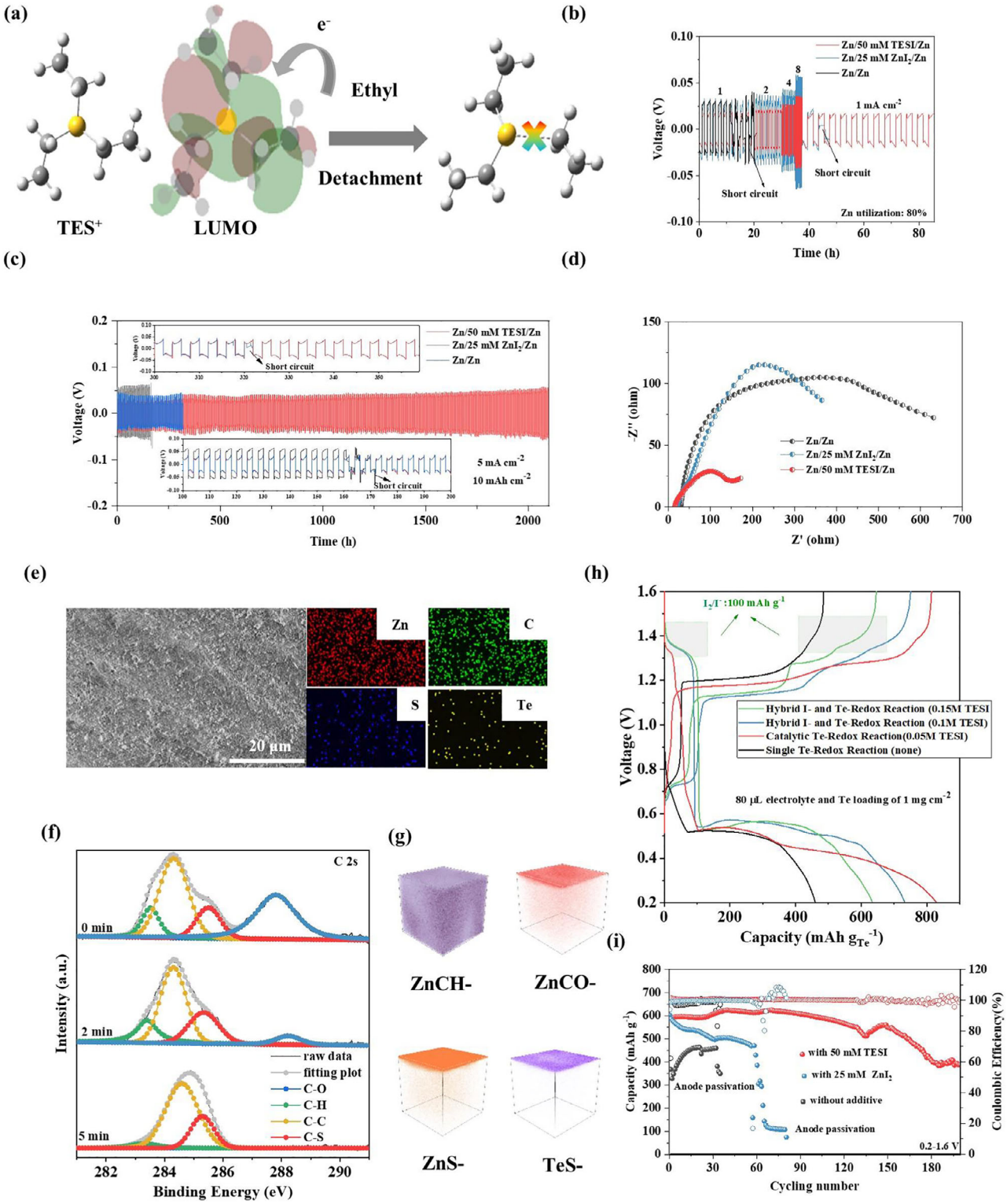

Figure 3. Facilitated anode SEI and cathode catalysis by TESI additives. a) Ethyl detaching mechanism of TES^+ to form C-rich SEI. b) Rate performance, c) long-term cycling test, and d) EIS spectra comparison of Zn/Zn anode after cycling utilizing different iodide additives. e) SEM images of SEI on Zn anode with elemental mapping. f) Fine C2s XPS spectra of SEI on zinc anode with different etching time and g) 3D TOF-SIMS mappings of the various species on the cycled Zn-metal surface in TESI electrolyte. h) GCD curves of aqueous Zn–Te battery with varied concentration of TESI at 0.3 A g^{-1} with Te loading of 1 mg (1 mg cm^{-2}). i) Cycling performance of aqueous Zn-Te battery at current density of 0.5 Ag^{-1} with different iodide additives and Te cathode loading of 5 mg cm^{-2}.

charge transfer.[46,47] Besides, the Te—I bond is a stable soft–soft interaction and has the highest covalent character among the Te–I, Te–Br, and Te–Cl.[1,2,37] Benefiting from this, the iodide additive is strategically effective in catalyzing an alternative electrochemical pathway that is intended to bypass it (Figure 2c). It is revealed that 50 mM TESI-derived I^- exhibits pronounced catalytic activity, as evidenced by the reduced voltage hysteresis and twofold capacity enhancement relative to additive-free electrolytes (Figure 3h; Figure S9a, Supporting Information). The iodide additive is also found to effectively catalyze a neutral Zinc-air battery and can prolong the cycling life of the zinc-air battery up to 110 times (Figure S10, Supporting Information). The reversibility of the Zn–Te battery is critically dependent on both the concentration and the total amount of iodide species. While iodide is essential for its catalytic role, excessive concentrations (>0.2 M) risk the formation of long-chain polyiodides (I_5^-, I_7^-). These species suffer from sluggish redox kinetics, leading to a lower output potential and severely compromised cyclability in aqueous Zn/iodide batteries (Figures S8b and S11a, Supporting Information). This detrimental aggregation is particularly pronounced when using inorganic iodides or high concentrations (Figure S11c, Supporting Information). In our system, TESI at concentrations ≤0.15 M strikes an effective balance, maintaining reversibility while contributing limited capacity (≈100 mAh g^{-1} at 0.15 M). More importantly, the organic TES^+ cation acts as a key stabilizer. In contrast to inorganic salts, it specifically suppresses long-chain growth and stabilizes the short-chain I_3^- species, thereby enhancing conversion kinetics and ensuring highly reversible electrochemistry even with a high total volume of low-concentration iodide (Figures S8b,S9d, and S11, Supporting Information).[48,49]To validate this inhibitory and catalytic effect under practical conditions, we tested Zn–Te full cells with high mass loading (>5 mg cm^{-2}) using an optimal TESI concentration of 50 mM (I^-/Te ≈7). With this formulation, the cells demonstrated stable performance even when the total solution volume was increased (Figure S9d, Supporting Information). Crucially, the iodine redox contribution remained negligible (< 50 mAh g^{-1}), confirming that the TESI additive functions primarily as a catalyst without inducing capacity-degrading shuttling phenomena (Figure 3h). As delineated in Figure 3i, the TESI-incorporated cell preserved a capacity of 386 mAh g^{-1} over 200 cycles at 0.5 A g^{-1}. Conversely, cells employing inorganic iodide additives exhibited diminished cycle stability (< 50 cycles), a consequence of ineffective catalysis and anode passivation triggered by persistent tellurium migration. In cycled Zn–Te batteries with TESI additive, the anode SEI is well maintained and cathode undergoes pulverization (Figure S12, Supporting Information). Despite initial stability, capacity retention degrades significantly and columbic efficiency fluctuates after 180 cycles. XRD and XPS analysis of the cycled Te electrode reveals unstable phase and composition during cycling. This indicates that the electro-catalytic process, while providing a lower activation barrier, cannot fully counteract persistent tellurium dissolution via non-equilibrium pathways (Figure S13, Supporting Information). Although the Le Chatelier principle allows for recycling of dissolved species, the net effect is a gradual but inevitable takeover by the proton tunneling mechanism, ultimately causing battery degradation (discuss later).[50]

The fundamental limitation of the electro-catalytic mechanism necessitates a paradigm shift from strategies focused solely on catalyzing reactions to autonomously synergistic repairing. Driven by the inherent potential difference between iodide anions (I^-) and $TeO_3{\cdot}H_2O$ molecules, spontaneous electron transfer from I^- to $TeO_3{\cdot}H_2O$ facilitates the reduction of dissolved tellurium species, effectively suppressing their shuttling behavior. This redox-mediated scavenging mechanism is schematically illustrated in **Figure** 4a; Figure S14c (Supporting Information). To enhance the absorption ability of dissolved species, we designed a copper single-atom (Cu_{SA}) substrate (Figure 4b; Figures S11a,b–S14, Supporting Information). Density functional theory (DFT) calculation was conducted first to delve into absorption energy of dissolved species. As compared in Figure 4b, triiodide anions, $TeO_2{\cdot}H_2O$, and $TeO_3{\cdot}H_2O$, are thermodynamically favored to be absorbed on Cu_{SA} substrate, thus promote the subsequent reduction reaction. It is further verified in Figure 4c that, compared to carbon substrate, Cu_{SA} exhibits more pronounced adsorption capacity toward I^-/I_3^-, with trace of I_3^- attributable to the aerial oxidation ($O_2 + 4I^- + 4H^+ \rightarrow 2I_2 + 2H_2O$) and instantaneous conversion ($I_2 + I^- \rightleftharpoons I_3^-$).[48,49]

To evaluate the long-term cycling stability and revitalization capability enabled by TESI, we conducted extended cycling tests of Zn–Te batteries at 2 A g^{-1} with periodic resting intervals. The batteries were systematically discharged to completion prior to each resting phase to ensure sufficient generation of triiodide anions for the regeneration process.

Because regeneration (H_2TeO_x(aq)→Te(s)) is a heterogeneous process (chemical reduction, nucleation and growth of solid Te). Each has its own rate constant. The actual fraction of Te recovered with time (hours) and TESI concentration is therefore determined experimentally. As shown in Figures S15 (Supporting Information), by 12 h, most soluble $H_mTe_nO_x$ (aq) (>90%) has already been reduced, leaving only dilute residues that are much slower to capture. Notably, the recovery disobeys pseudo-first-order kinetics and iodine content remains stable throughout the recovery process, support the sustainability and satisfactory recyclability of proposed loop chemistry. Waiting longer (24 h) only add a few percent extra recovery but doubles the time cost. Thus, 12 h is chosen as the benchmark for practical completion of the process (t_{90} point) where further waiting yields diminishing returns.[51]

Long-term cycling tests of Zn–Te batteries at 2 A g^{-1} with 12 and 24-h resting were carried out, with Te mass loading 5 mg at 5 mg cm^{-2}. Without adding TESI, the capacity of the Zn-Te battery shows a steadily decreasing trend in the first 150 cycles (Figure 4d). Even after resting for 12 and 24 h, the Zn–Te battery still suffers capacity fading over the carbon substrate. In sharp contrast, after cycling the Zn–Te battery with 50 mM TESI for 1500 cycles, it can recover a capacity of up to 424 mAh g^{-1} (93.3% of the initial capacity) after 12 h of sleeping (Figure 4e). Following an additional 400 cycles, a subsequent 24-h resting period enabled the Zn–Te battery to recover a reversible capacity of 412 mAh g^{-1}, demonstrating the remarkable self-healing capability of the system through TESI-mediated regeneration. To enhance the adsorption of dissolved tellurium species, we replaced the conventional carbon substrate with a Cu single-atom catalyst. As evidenced in Figure 4f, this modification significantly improved the electrochemical performance, with the Zn–Te battery maintaining 56% capacity after 1500 cycles, a substantial enhancement compared to the mere 20.7% retention observed

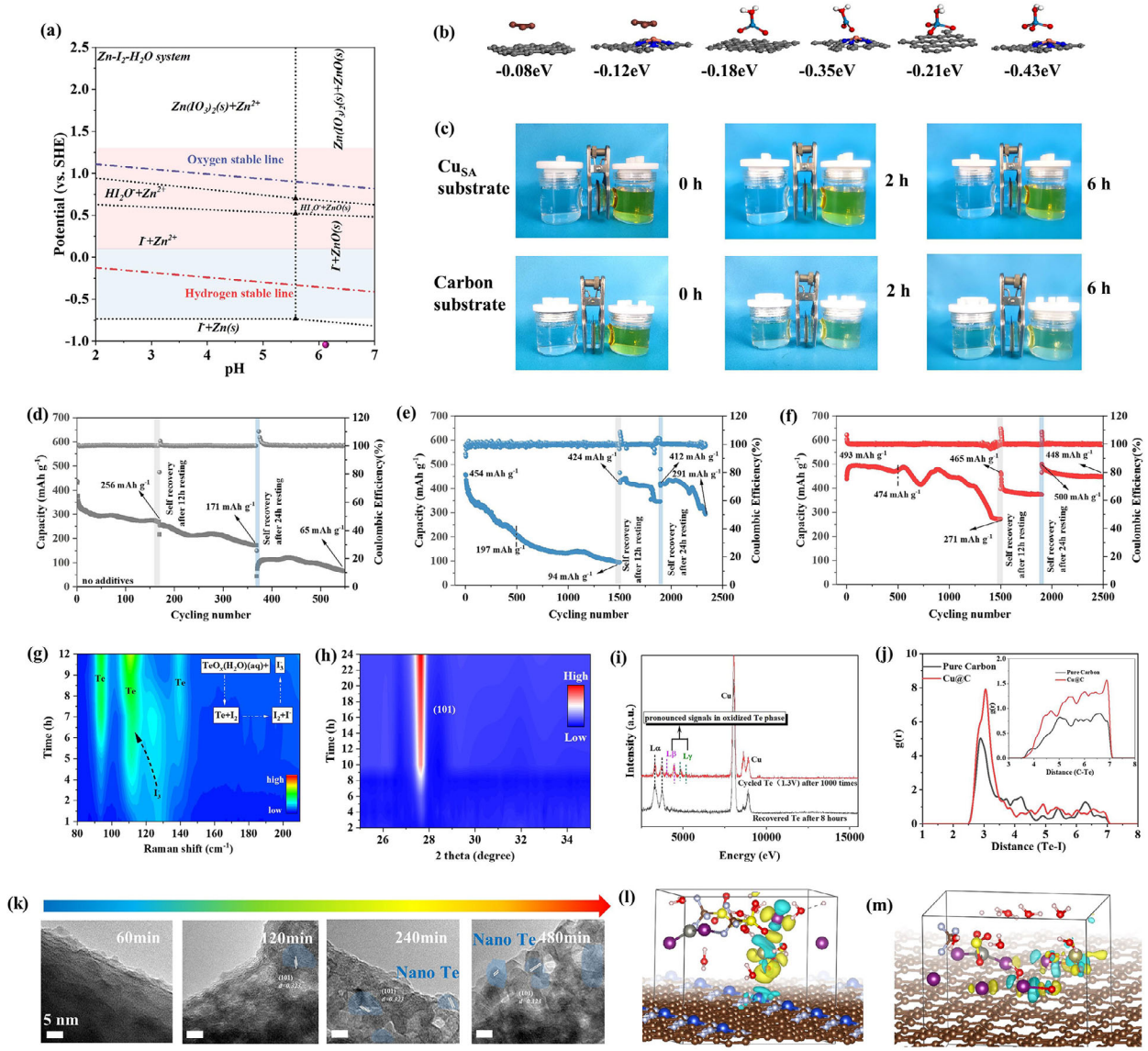

Figure 4. Self-rejuvenating via cathode loop chemistry. a) Pourbaix diagram of Zn-Iodine-H_2O system. b) Absorption energy of triple iodide, $TeO_2{\cdot}H_2O$, and $TeO_3{\cdot}H_2O$ on carbon substrate and Cu single-atom substrate. c) Digital images of I^-/I_3^- diffusion and adsorption behavior in 0.2 M TESI/2 M $ZnSO_4$ solution with Carbon, Cu_{SA} substrate for 6 h (left chamber: 2 M $ZnSO_4$; right chamber: 0.2 M TESI/2 M $ZnSO_4$). Long-term cycling test of Zn-Te battery d) without TESI additive and with 50 mM TESI additive over e) carbon substrate and f) Cu_{SA} substrate. The aqueous Zn–Te batteries were fully discharged before resting for hours. g) In situ Raman spectra and h) In situ XRD pattern of recovering process of degraded Te cathode over Cu_{SA} substrate. i) TEM-EDS of cycled Te and recovered Te via loop chemistry. j) RDF of C-Te and obtained from molecular dynamic simulation (inset: RDF of I-Te). k) Ex situ high-resolution TEM images of rejuvenated Te evolved with time. Charge-density difference plot of interfacial $TeO_x{\cdot}H_2O$-I_3^- over l) carbon and m) Cu_{SA} substrate.

with the carbon substrate. The system demonstrated exceptional regenerative capabilities, recovering 94.1% of its initial capacity (464 mAh g^{-1}) following a 12-h resting period. Subsequent cycling for 400 additional cycles resulted in a gradual capacity loss of ≈94 mAh g^{-1}, yet after a 24-h recovery period, the battery remarkably regained 500 mAh g^{-1} while maintaining stable redox characteristics (Figure S16, Supporting Information).

To elucidate the exceptional capacity recovery mechanism, we conducted comprehensive characterization using in situ Raman spectroscopy, in situ XRD, and first-principles molecular dynamics (MD) simulations. These investigations employed a fully degraded Te cathode with residual capacity below 50 mAh g^{-1}. The in situ Raman spectra (Figure 4g) reveal critical insights into the regeneration process: initially, only a weak signal at ≈126 cm^{-1}, corresponding to triiodide anion vibrations, is detectable at the cathode-electrolyte interface. Over time, this triiodide peak intensifies and undergoes a distinct redshift, while three additional vibrational modes emerge at 93.9, 112, and 140 cm^{-1}, characteristic of reactivated Te species. These spectral evolutions demonstrate a strong interfacial interaction between triiodide

anions and tellurium species, facilitating the reduction of dissolved $TeO_3 \cdot H_2O$ through electron tunneling. The redox cycle is completed through the regeneration of triiodide anions via iodine recycling, where generated I_2 reacts with iodide anions to regenerate the active I_3^- species.[29–31] Additionally, a gradual intensification of the XRD peak at ≈27.6° in the in situ XRD pattern reveals the regeneration of the crystalline Te phase (Figure 4h). By increasing the concentration of TESI, the ex situ XRD pattern shows a pronounced diffraction of iodine accompanied by the formation of $(Zn(OH)_2)_3(ZnSO_4)(H_2O)$(s), which suggests the participation of protons in the loop chemistry (Figure S17a, Supporting Information). Additionally, ex situ Te 3d XPS analysis shows that the revitalized Te phase exhibits characteristics close to Te(0) (Figure S17c, Supporting Information).

The regenerated phase was specifically investigated using HRTEM. As shown in Figure 4k, prolonged resting time induces recrystallization of the Te-dominated phase from the electrolyte. As confirmed by TEM-EDS profile (Figure 4i), cycled Te display three peaks (3.3–3.7, 4–4.5, and 4.8–5.2 keV), evidencing multiple oxidized Te species (TeO_x, $H_xTe_mO_n$). In contrast, iodide-recovered Te shows a dominant 3.3–3.7 keV peak with only a minor 4–4.5 keV signal, confirming reduction of high-valence species back to Te^0. To unravel the molecular interactions driving this redox behavior, MD simulations were performed. The radial distribution functions (RDFs) in Figure 4j demonstrate intensified C–Te and I–Te interactions for the Cu_{SA} catalyst compared to pure carbon substrates, indicating stronger adsorption of Te species and iodide anions on Cu single-atom sites. Complementary charge density difference (Figure 4l,m) and density of states (DOS) analysis (Figures S18, Supporting Information) reveal enhanced orbital hybridization between Te species, iodide anions, and Cu_{SA} substrate, facilitating electron transfer that promotes Te reduction. Notably, water molecules participate in this electron migration, acting as proton donors. Based on these findings, the regenerative electrochemical loop can be described as:

$$H_2O = H^+ + OH^- \quad (6)$$

$$4Zn^{2+} + 6OH^- + SO_4^{2-} + H_2O = (Zn(OH)_2)_3(ZnSO_4)(H_2O)\,(s) \quad (7)$$

$$TeO_3 \cdot H_2O\,(aq) + 6I_{3^-} + 6H^+ = 9I_2 + Te\,(s) + 4H_2O \quad (8)$$

$$I_2 + I^- = I_{3^-} \quad (9)$$

During the charging process in the presence of TESI, the continuous generation of protons shifts the equilibrium of the recycling reaction to the right, in accordance with Le Chatelier's principle.[50] This shift promotes the dynamic regeneration of solid tellurium (Te(s)) from dissolved $TeO_x \cdot H_2O$(aq), thereby counterbalancing dissolution-induced active material loss and enabling long-term deep cycling stability. The net gain of active material from this chemical regeneration during the charging phase also explains the observed coulombic efficiency (CE) exceeding 100% (Figure 4e,f).

For practical evaluation, pouch cells were prepared with a high mass loading of 10 mg cm^{-2} using the lamination technique, and a negative to positive (N/P) ratio controlled at 5:1. The use of TESI as a triple functional additive could extend cycle life to 80 cycles with high capacity retention of 81.4% at a current density of 3 mA cm^{-2} without passivation tellurium shuttling (**Figure 5a**), and no noticeable swelling is observed after the cycling test. The effectiveness of loop chemistry to regenerate a degraded Te cathode was further assessed in the pouch cell. The pouch cell has an initial capacity of 30 mAh at 1 mA cm^{-2}, which gradually fades during 135 cycles to 18.2 mAh. Following a 24-h resting period, the cell exhibited a significant capacity recovery of 28.9 mAh (Figure 5b), demonstrating the reversibility of capacity fade through electrochemical self-repair mechanisms. Three Zn–Te batteries connected in series were used to demonstrate the successful powering of an electrochromic device (Figure 5c). Overall, our loop chemistry could efficiently regenerate the Te cathode without consuming energy, outperforming previously reported cathode regeneration approaches (Figure 5d; Table S5, Supporting Information).[52–55]

3. Conclusion

A key challenge in realizing the full potential of aqueous Zn–Te batteries lie in the paradoxical role of electrochemical hydrolysis: while PCET-driven equilibrium reactions enable high-capacity redox, dynamic proton tunneling diverts these processes into non-equilibrium pathways that cause $TeO_x \cdot H_2O$ (aq) shuttling. The same non-equilibrium mechanism explains uncontrolled Mn^{2+} redeposition in Zn–MnO_2 battery and the formation of high-valence $Zn(OH)_2 \cdot V_2O_7 \cdot nH_2O$ in Zn–V_2O_5 battery. This study addresses the critical $TeO_x \cdot H_2O$(aq) shuttling in Zn–Te batteries through a closed-loop chemistry enabled by TESI. Despite iodide anions catalyzing tellurium conversion with a lower activation barrier, the reaction is progressively overtaken by a shuttle mechanism during cycling enabled by quantum mechanical proton tunneling. A regenerative chemistry is simultaneously introduced to overcome electro-catalytic limitations: triiodide anions reduce dissolved Te species, rejuvenating the cathode, while the I_2 generated during this reduction reaction is recycled back into the electrolyte through a reaction with iodide anions, closing the chemical loop and minimizing the loss of active components. Additionally, TES^+ forms a protective SEI on the zinc anode, preventing passivation and dendrite growth. This strategy enables remarkable battery rejuvenation (recovering 94.3% of capacity, 465 mAh g^{-1}, after 1500 cycles by simply resting for 12 h) and extends operational lifespan by simultaneously stabilizing both electrodes. Beyond device performance, these findings provide a generalizable fading mechanism for multiple aqueous Zn systems (Te, MnO_2, V_2O_5): equilibrium reaction pathways are diverted by proton tunneling. Importantly, this model reconciles previously inconsistent in situ and ex situ observations, showing that both capture correct but temporally distinct stages of dynamic degradation. By providing a unified mechanistic framework, our findings not only elucidate fundamental degradation pathways across multiple aqueous zinc-ion systems but also guide the rational design of regenerative chemistries and durable battery architectures.

4. Experimental Section

Synthesis of Cu Single-Atom Catalyst: Zn acetylacetonate (1054 mg) and dimethylimidazole (1314 mg) were uniformly blended with copper acetylacetonate (2 mg) through mechanical grinding. The mixture

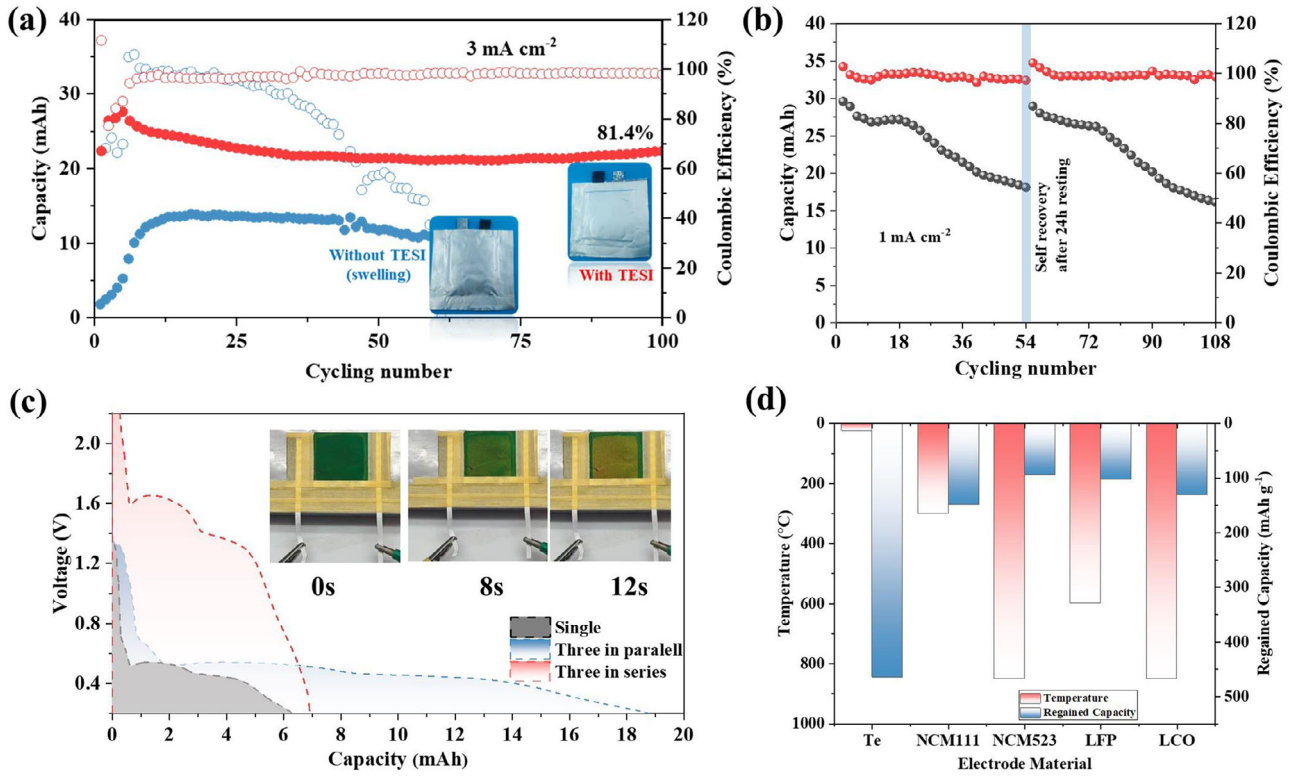

Figure 5. a) Cycling performance of pouch aqueous Zn–Te battery. Inset: image of cycled pouch cells with or without TESI. b) Self-recovering performance of pouch aqueous Zn-Te battery with TESI additive. c) Discharge curve of three aqueous Zn–Te batteries connected in parallel and series. Inset: images of battery-driven electrochromic device. d) Comparison of our application of cathode-loop revitalizing chemistry to Te with other reported regenerated materials.

underwent stepwise thermal treatment under nitrogen atmosphere, involving sequential ramping from ambient temperature to 100 °C (30 min), holding at 100 °C (20 min), controlled heating to 200 °C (60 min), maintaining at 200 °C (140 min), ramping to 900 °C (60 min), and final stabilization at 900 °C (60 min).

Synthesis of Te Electrode: Te powder was obtained via hydrothermal reaction ($N_2H_4 \rightarrow N_2 + 4H^+ + 4e^-$; $4e^- + 6H^+ + Na_2TeO_3 \rightarrow Te + 3H_2O+2Na^+$). The cathode fabrication process began by combining Te powder, acetylene black, and PVDF binder in a 7:2:1 mass ratio. These components were blended in ethanol to create a uniform slurry, which was subsequently coated onto a carbon cloth substrate. The coated substrate was vacuum-dried at 80 °C overnight to remove solvents. The mass loading of the active material on the cathode was maintained at ≈5 mg cm^{-2}.

Supporting Information

Supporting Information is available from the Wiley Online Library or from the author.

Acknowledgements

R.P. and Y.X. contributed equally to this work. This work was supported by the National Natural Science Foundation of China (52473270, T2422028, 12174050, and T2321002), the National Key R&D Program of China (2022YFA1203304), the Natural Science Foundation of Jiangsu Province (BK20231411 and BK20222007), the Suzhou Institute of Nano Tech and Nano Bionics, Chinese Academy of Sciences (Start up grant E1552102). The authors are grateful for the technical support of TOF-SIMS by Rong Huang for Nano-X Suzhou Institute of Nano-Tech and Nano-Bionics, Chinese Academy of Sciences.

Conflict of Interest

The authors declare no conflict of interest.

Data Availability Statement

The data that support the findings of this study are available from the corresponding author upon reasonable request.

Keywords

non-equilibrium dynamic pathways, proton tunneling, regenerative chemistry, sustainable aqueous zinc-ion battery, tellurium shuttle

Received: October 9, 2025
Revised: November 4, 2025
Published online: November 17, 2025

[1] J. Qi, Y. Tang, Y. Wei, G. Liu, J. Yan, Z. Feng, Z. Han, M. Ye, W. Du, Q. Yang, Y. Zhang, Z. Wen, X. Liu, C. C. Li, *Energy Environ. Sci.* **2025**, *18*, 807.
[2] J. Du, Y. Zhao, X. Chu, G. Wang, C. Neumann, H. Xu, X. Li, M. Löffler, Q. Lu, J. Zhang, D. Li, J. Zou, D. Mikhailova, A. Turchanin, X. Feng, M. Yu, *Adv. Mater.* **2024**, *36*, 2313621.
[3] B. D. Adams, V. Duffort, S. H. Vajargah, L. F. Nazar, *Nat. Energy* **2016**, *1*, 1.

[4] J. Li, H. Liu, H. Zhang, S. Xi, Z. Zhu, *Angew. Chem., Int. Ed.* **2023**, *135*, 202312000.
[5] Z. Chen, C. Zhi, *Nat. Rev. Mater.* **2025**, *10*, 268.
[6] R. Pan, Y. Xie, B. Jiang, T. Liu, Y. Han, Z. Shao, A. Cabot, S. Jiao, L. Sun, K. Yin, Q. Zhang, *Adv. Mater.* **2025**, *37*, 2512633.
[7] Z. Jiang, Y. Zhang, D. B. Ravnsbæk, C. Gao, N. B. Christensen, F. Cui, R. Pan, K. Luo, G. Zhang, W. Zhang, S. Lei, L. Sun, G. He, K. Yin, Y. Yue, *Adv. Mater.* **2024**, *36*, 2413167.
[8] Y. Fu, Z. Wu, Y. Yuan, P. Chen, L. Yu, L. Yuan, Q. Han, Y. Lan, W. Bai, E. Kan, *Nat. Commun.* **2020**, *11*, 845.
[9] Y. Qiao, Z. Chang, X. Cao, M. Jia, P. He, H. Zhou, *Angew. Chem., Int. Ed.* **2019**, *58*, 11774.
[10] X. Hu, J. Li, G. Zhong, J. Yuan, H. Zhan, Y. Tang, Z. Wen, *Nat. Commun.* **2022**, *13*, 663.
[11] S. Zhou, J. Shi, S. Liu, G. Li, F. Pei, Y. Chen, J. Deng, Q. Zheng, J. Li, C. Zhao, I. Hwang, C.-J. Sun, Y. Liu, Y. Deng, L. Huang, Y. Qiao, G.-L. Xu, J.-F. Chen, K. Amine, S.-G. Sun, H.-G. Liao, *Nature* **2023**, *621*, 75.
[12] J. Li, C. Lei, P. Jiang, C. Xu, T. Liu, X. Liang, *Energy Environ. Sci.* **2024**, *17*, 8633.
[13] Q. Pang, J. Meng, S. Gupta, X. Hong, C. Y. Kwok, J. Zhao, Y. Jin, L. Xu, O. Karahan, Z. Wang, *Nature* **2022**, *608*, 704.
[14] Z. Yu, W. Wang, Y. Zhu, W.-L. Song, Z. Huang, Z. Wang, S. Jiao, *Nat. Commun.* **2023**, *14*, 5596.
[15] P. Halli, B. P. Wilson, T. Hailemariam, P. Latostenmaa, K. Yliniemi, M. Lundström, *J. Appl. Electrochem.* **2020**, *50*, 1.
[16] S. Wang, Z. Wei, H. Hong, X. Guo, Y. Wang, Z. Chen, D. Zhang, X. Zhang, X. Yang, C. Zhi, *Nat. Commun.* **2025**, *16*, 511.
[17] J. Si, Y. Sun, R. Qi, Q. Lei, W. Zhang, Z. Ren, Y. Zhao, H. Li, M. Lin, W. Wen, *Adv. Energy Mater.* **2024**, *14*, 2303982.
[18] J. Li, L. Zhang, W. Xin, M. Yang, H. Peng, Y. Geng, L. Yang, Z. Yan, Z. Zhu, *Small* **2023**, *19*, 2304916.
[19] H. Xu, H. Liu, W. Yang, M. Li, F. Zhao, C. Li, J. Qi, H. Wang, W. Peng, X. Fan, *Chem. Eng. J.* **2024**, *485*, 149825.
[20] R. Pan, F. Cui, A. Zheng, G. Zhang, Z. Jiang, Y. Xiong, L. Wei, Q. Zhang, L. Sun, K. Yin, *Adv. Funct. Mater.* **2023**, *33*, 2300619.
[21] J. Liu, C. Ye, H. Wu, M. Jaroniec, S.-Z. Qiao, *J. Am. Chem. Soc.* **2023**, *145*, 5384.
[22] X. Yu, T. Zhang, Y. Feng, X. Li, J. Zhang, J. Mi, C. Ye, W. Li, D. Zhao, D. Chao, *Adv. Mater.* **2025**, *37*, 07561.
[23] F. Cui, R. Pan, L. Su, C. Zhu, H. Lin, R. Lian, R. Fu, G. Zhang, Z. Jiang, X. Hu, Y. Pan, S. Hou, F. Zhang, K. Zhu, Y. Dong, F. Xu, *Adv. Mater.* **2023**, *35*, 2306580.
[24] N. Zhang, F. Cheng, J. Liu, L. Wang, X. Long, X. Liu, F. Li, J. Chen, *Nat. Commun.* **2017**, *8*, 405.
[25] H. Pan, Y. Shao, P. Yan, Y. Cheng, K. S. Han, Z. Nie, C. Wang, J. Yang, X. Li, P. Bhattacharya, K. T. Mueller, J. Liu, *Nat. Energy* **2016**, *1*, 16039.
[26] Y. Yuan, R. Sharpe, K. He, C. Li, M. T. Saray, T. Liu, W. Yao, M. Cheng, H. Jin, S. Wang, K. Amine, R. Shahbazian-Yassar, M. S. Islam, J. Lu, *Nat. Sustain.* **2022**, *5*, 890.
[27] C. Zhong, B. Liu, J. Ding, X. Liu, Y. Zhong, Y. Li, C. Sun, X. Han, Y. Deng, N. Zhao, W. Hu, *Nat. Energy* **2020**, *5*, 440.
[28] W. Sun, F. Wang, S. Hou, C. Yang, X. Fan, Z. Ma, T. Gao, F. Han, R. Hu, M. Zhu, C. Wang, *J. Am. Chem. Soc.* **2017**, *139*, 9775.
[29] J. Huang, Z. Wang, M. Hou, X. Dong, Y. Liu, Y. Wang, Y. Xia, *Nat. Commun.* **2018**, *9*, 2906.
[30] N. B. Lewis, R. P. Bisbey, K. S. Westendorff, A. V. Soudackov, Y. Surendranath, *Nat. Chem.* **2024**, *16*, 343.
[31] S. Fatima, L. Olshansky, *Nat. Rev. Chem.* **2024**, *8*, 762.
[32] P. Garrido-Barros, J. Derosa, M. J. Chalkley, J. C. Peters, *Nature* **2022**, *609*, 71.
[33] X. Meng, J. Guo, J. Peng, J. Chen, Z. Wang, J. R. Shi, X. Z. Li, E.-G. Wang, Y. Jiang, *Nat. Phys.* **2015**, *11*, 235.
[34] G. A. Parada, Z. K. Goldsmith, S. Kolmar, B. Pettersson Rimgard, B. Q. Mercado, L. Hammarström, S. Hammes-Schiffer, J. M. Mayer, *Science* **2019**, *364*, 471.
[35] O. Jung, M. N. Jackson, R. P. Bisbey, N. E. Kogan, Y. Surendranath, *Joule* **2022**, *6*, 476.
[36] Y. Zhang, W. Zhou, B. Wang, T. Zhang, X. Yu, X. Li, G. Li, H. Jin, M. Chen, W. Li, D. Zhao, X. Liu, D. Chao, *Angew. Chem., Int. Ed.* **2025**, *64*, 202424056.
[37] Z. Chen, S. Wang, Z. Wei, Y. Wang, Z. Wu, Y. Hou, J. Zhu, Y. Wang, G. Liang, Z. Huang, *J. Am. Chem. Soc.* **2023**, *145*, 20521.
[38] J. Qi, Y. Tang, Z. Feng, J. Yan, G. Liu, M. Ye, W. Du, Q. Yang, Y. Wei, Y. Zhang, *Adv. Ener. Mater.* **2024**, *14*, 2303616.
[39] R. Pan, A. Zheng, B. He, Y. Xiong, F. Han, L. Wei, Q. Li, Q. Zhang, K. Yin, L. Sun, *Nanoscale Horiz.* **2022**, *7*, 1501.
[40] L. Wang, K.-W. Huang, J. Chen, J. Zheng, *Sci. Adv.* **2019**, *5*, aax4279.
[41] B. Wu, X. Liu, P. Liu, G. Wu, L. Tian, X. Han, J. Li, X. Hong, *Nat. Synth.* **2025**, *1*, 1.
[42] C. Zhao, C. Tan, D.-H. Lien, X. Song, M. Amani, M. Hettick, H. Y. Y. Nyein, Z. Yuan, L. Li, M. C. Scott, A. Javey, *Nat. Nanotechnol.* **2020**, *15*, 53.
[43] C. Cassidy, *Micron* **2025**, *198*, 103875.
[44] D. Kundu, S. H. Vajargah, L. Wan, B. Adams, D. Prendergast, L. F. Nazar, *Energy Environ. Sci.* **2018**, *11*, 881.
[45] C. T. Wolke, J. A. Fournier, L. C. Dzugan, M. R. Fagiani, T. T. Odbadrakh, H. Knorke, K. D. Jordan, A. B. McCoy, K. R. Asmis, M. A. Johnson, *Science* **2016**, *354*, 1131.
[46] W. Yao, J. Xu, L. Ma, X. Lu, D. Luo, J. Qian, L. Zhan, I. Manke, C. Yang, P. Adelhelm, *Adv. Mater.* **2023**, *35*, 2212116.
[47] W. Wu, S. Wang, L. Lin, H. Y. Shi, X. Sun, *Energy Environ. Sci.* **2023**, *16*, 4326.
[48] G. Choi, P. Sullivan, X.-L. Lv, W. Li, K. Lee, H. Kong, S. Gessler, J. R. Schmidt, D. Feng, *Nature* **2024**, *635*, 89.
[49] W. Zhong, H. Cheng, S. Zhang, L. Li, C. Tan, W. Chen, Y. Lu, *Nat. Commun.* **2025**, *16*, 4586.
[50] H. Li, R. Meng, C. Ye, A. Tadich, W. Hua, Q. Gu, B. Johannessen, X. Chen, K. Davey, S.-Z. Qiao, *Nat. Nanotechnol.* **2024**, *19*, 792.
[51] D. van der Zwaag, P. A. Pieters, P. A. Korevaar, A. J. Markvoort, A. J. H. Spiering, T. F. A. de Greef, E. W. Meijer, *J. Am. Chem. Soc.* **2015**, *137*, 12677.
[52] T. Yang, D. Luo, X. Zhang, S. Gao, R. Gao, Q. Ma, H. W. Park, T. Or, Y. Zhang, Z. Chen, *Nat. Sustain.* **2024**, *7*, 776.
[53] J. Wang, K. Jia, J. Ma, Z. Liang, Z. Zhuang, Y. Zhao, B. Li, G. Zhou, H.-M. Cheng, *Nat. Sustain.* **2023**, *6*, 797.
[54] H. Ji, J. Wang, J. Ma, H.-M. Cheng, G. Zhou, *Chem. Soc. Rev.* **2023**, *52*, 8194.
[55] Y. Hu, M. Yang, Q. Dong, X. Zou, J. Yu, S. Guo, F. Yan, *Energy Environ. Sci.* **2024**, *17*, 4238.